High-fidelity simulation of an aerated cavity around a surface-piercing rectangular plate

Yiding Hu,[1] Cheng Liu,[1,*] Min Zhao,[1] and Changhong Hu[2]
[1]*School of Naval Architecture, Ocean and Civil Engineering, Shanghai Jiao Tong University, Shanghai 200240, China*
[2]*Research Institute for Applied Mechanics, Kyushu University, Fukuoka 816-0811, Japan*

(Received 30 October 2022; accepted 28 March 2023; published 27 April 2023)

A bluff body advancing through the water surface at high Froude number produces intricate two-phase flow patterns. One intuitive feature is an entrapped air cavity which subsequently breaks apart into a mass of droplets and bubbles. The bluff-induced cavity partially accounts for the appearance of bubble clouds in the wake. However, few experimental or numerical studies have been devoted to this phenomenon. To clarify this mechanism, high-fidelity simulations are performed to emphasize the evolution of the aerated cavity generated by a surface-piercing rectangular plate. First, the mesh independency study is performed to validate the trend of the convergence of the time-averaged wave profile, the bubble size distribution, the bubble number density, and the entrapped bubble volume. Then the formation and development of the aerated cavity induced by a surface-piercing plate with various yaw angles ($\alpha_E \in [10^\circ, 50^\circ]$) are investigated. Numerical simulations show that the air pocket is entrapped and develops with stabilized rotational motion, and the subsequent breakup of the air pocket constitutes the leading cause of the bubbly wake. The geometrical characteristics of the aerated rotation cavity are summarized as a function of yaw angles. Moreover, with the adaptive mesh strategy and high-resolution schemes, all the bubbles of equivalent radius $r \geqslant 2$ mm are captured and tracked, so the spatial and size distribution laws of the varying-sized bubbles pinching off from the air cavity in the wake are summed up. In addition, large-scale coherent structures wrapped around the cavity and the effects on air entrainment are discussed.

DOI: 10.1103/PhysRevFluids.8.044003

I. INTRODUCTION

The bubbly wake behind a surface-piercing structure is a commonly observed phenomenon in hydrodynamics. Many experimental or numerical works have been performed to reveal the physical mechanisms of surface-piercing flows, induced by various structures (e.g., flat plate [1–4], hydrofoil [5], cylinder [6], wedge-shaped bow [7–10], and rectangular stern [11–13]). The high-fidelity simulation of breaking bow waves by a surface-piercing flat plate has recently been performed (Hu *et al.*) [4]. As shown in Fig. 1, our numerical simulation indicates that a large-scale aerated pocket with a conical shape is formed at the fringe of the plate. Moreover, the conical air cavity shows a stabilized rotation at the leading end. With the development of flow instability, the cavity cannot maintain a conical shape, the interface is distorted, and bubbles of various sizes are formulated. In this paper, we aim to analyze the flow structure of the aerated cavity in detail and perform a quantitative investigation to explore the role of these structures in air entrainment.

*chengliu@sjtu.edu.cn

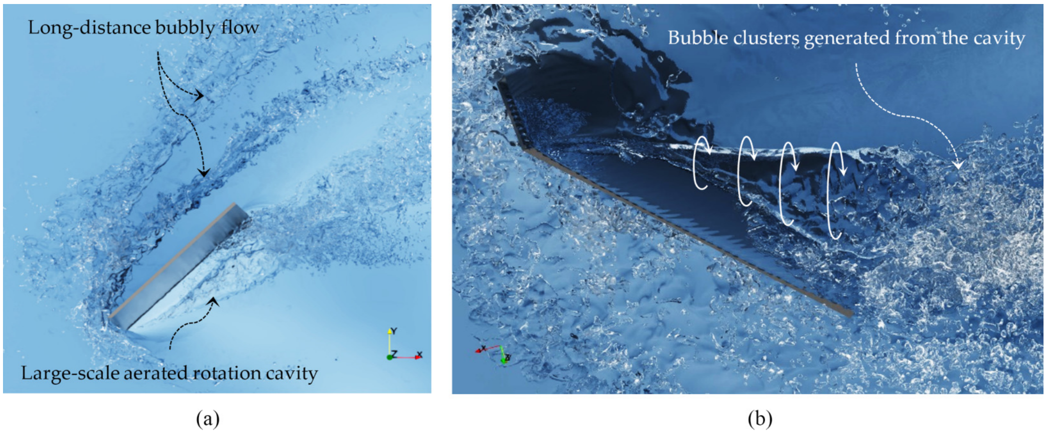

FIG. 1. Bow wave breaking is generated by a surface-piercing flat plate, revealing an aerated rotation cavity. As the bow wave breaks, air is entrained and carried along, leading to the generation of a large-scale air pocket. At the tail of the cavity, bubble clusters are pinched off from it. (a) Top view. (b) Bottom view.

There is much experimental and numerical research on air cavity for the cases of plunging jet and canonical wave breaking. Gomez-Ledesma *et al.* [14] conducted a nice experiment on the impact of a translating plunging jet on a pool, which creates an air cavity. Then three examples of cavities in the experiment were compared and analyzed in terms of air entrainment by Clanet [15]. However, due to the strong interactions between free-surface aeration and turbulence, the quantitative analysis is challengeable. A detailed description of these structures is not available using experimental measurements due to technical difficulties. Recently, significant attention has been devoted to a large-scale air cavity in plunging wave breaking via high-fidelity simulations with very large grids (up to billions of grid points). In the study of Wang *et al.* [16], the spanwise three-dimensional (3D) interfacial structures of an air cavity were presented and its flow instability was investigated by the cross-section velocity and vortex fields. Mostert *et al.* [17] discussed the shape of the cavity with different Bond and Reynold numbers and provided a correction for the scaling of the entrapped volume. Gao *et al.* [18] investigated the breakup procedure from the air cavity to bubbles due to the unstable growth of interfacial waves, while research on the air cavity induced by a surface-piercing structure is rare. The aerated cavity of the surface-piercing flat plate is analogous to the air cavity entrapped by plunging breakers, but the detailed flow characteristics are completely different. For instance, the leading-edge cavity in this paper is a quasisteady rotating process and develops into a steady state ultimately. It is an energy-input process, which is like the air cavity owing to the impact of a translating plunging jet on a pool, while the air cavity formulated in the plunging breakers usually experiences a short period of residence and breaks up into bubbles within a few seconds [16,19]. Moreover, the two types of air cavity also show geometrical differences: a conical shape for the leading-edge cavity and a cylindrical shape for the breaking waves [18]. It is noted that, for the plunging breaker, the cavity will be completely converted into an array of bubbles [18], while for the surface-piercing plate in this paper, the conical cavity breaks only at the tail.

The air cavity is a typical multiphase flow, which is responsible for the accumulation of many bubbles by its breakup and interacting with the free surface. Thus, it is significant to accurately describe the air entrainment process. The entrainment process of the air cavity has been well studied for the cases of the liquid jet impact [20,21] and plunging breakers [22,23]. For example, several principles of air entrainment, including the jet impact entrainment, the splash-impact entrainment, and turbulent entrainment in plunging jet and breaking waves, were demonstrated in detail by Kiger and Duncan [23]. Meanwhile, the air entrainment process results in bubble clustering (foam) floating on the free surface [24], as shown in Fig. 1. One of the most important quantities to characterize

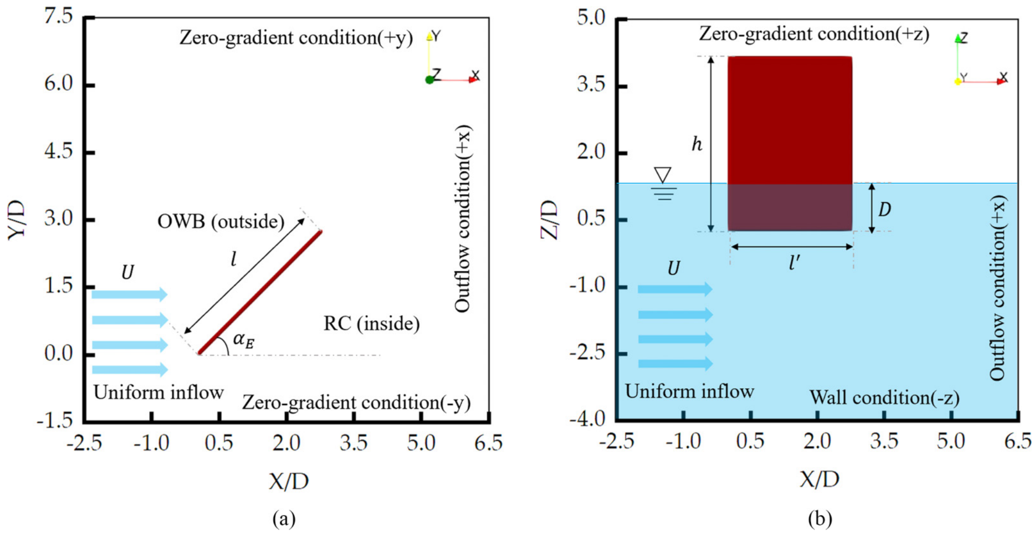

FIG. 2. Schematic of the computational domain. (a) Top view (x-y plane). (b) Side view (x-z plane). The outside and inside of the plate are indicated by the overturning wave breaking (OWB) and the rotation cavity (RC) regions, respectively.

the air entrainment is the spectrum of bubble sizes. A widely used turbulent breakup cascade model was provided by Garrett *et al.* [25] for assessing the bubble size distribution, following a power-law scaling with a slope of $-\frac{10}{3}$. Deane and Stokes [26,27] confirmed the $-\frac{10}{3}$ power law for the bubbles beyond the Hinze scale (≈ 2 mm) and extended another pattern for bubbles below the Hinze scale with a slope of $-\frac{2}{3}$ by the experimental study. Recently, Chan *et al.* [28–30] focused on microbubbles and reproduced the bubble-mass cascade by direct numerical simulation (DNS) of the breaking wave. These studies provide a valuable reference for the quantitative statistics of the bubbles in the wake.

3D organized large-scale coherent structures can be observed as the air cavity rotates due to the high circulation of water surrounding it, which are crucial for air entrainment. Similarly, in the study of Lubin *et al.* [31], fine streamwise vortex filaments were found under the air pocket at the early stage of wave breaking, and the evolution of large, aerated vortex filaments was described in detail. Many discussions about the generation of complicated 3D turbulent structures and their interactions were conducted by prior numerical works, which revealed further physical details regarding turbulent structures and yielded insight on air entrainment. Watanabe *et al.* [32] demonstrated the formation of large-scale 3D vortex structures in both plunging and spilling breakers by large-eddy simulation (LES) and investigated the interactions between bubbles and vortex structures. A series of pictures of air-liquid coherent structures related to surface deformations are presented in the work of Lakehal and Liovic [33] In terms of air entrainment induced by vortex structures, Yu *et al.* [34] investigated two kinds of typical free surface vortex connections in detail by DNS of a shear flow free surface. These studies of the interactions between vortex structures and the free surface improve our understanding of such interactions and bring further insights for this paper.

In a previous study [4], the bow wave (including the wave breaking and the resulting air entrainment) in the overturning wave breaking (OWB) region rather than the rotation cavity (RC) region [see Fig. 2(a)] was discussed in detail. The wave and air entrainment characteristics are compared with experimental observations and measurements [35–37] to verify the numerical results. From the high-fidelity simulations, we found that, in the RC region, the large-scale air pocket (appears in leading edge of the plate) and the associated bubbles generated by it contribute much more air entrainment in the wake than that of the bow wave breaking. Additionally, we found the formulation and dynamics of the leading-edge cavity are very different from the cavity caused by plunging jet (usually in the process of wave breaking). Since the aerated air cavity plays an important role in the generation of bubbly wake and is rarely discussed in existing studies, we perform an intensive investigation of the leading-edge cavity in this paper as an important complement. In this paper, we try to clarify the mechanisms involved in the formation of the aerated rotating cavity for the large yaw angles ($\alpha_E \geqslant 35^\circ$) and describe the main features of the air cavity, the subsequent breakup of the air pocket, and the characteristics of the associated bubbles in the wake.

The research highlights of this paper are briefly described as follows:

(1) This paper is an endeavor to employ high-fidelity numerical simulation for the quantitative study of the surface-piercing structure-induced cavity. By introducing the adaptive mesh refinement strategy and the high-resolution scheme, bubbles of various scales are resolved and tracked.

(2) We perform a quantitative analysis of the associated bubble and reveal that, in the process of the flow around the semisubmerged structure of a blunt body such as a flat plate, the large-scale cavity contributes the majority of air entrainment in the wake.

(3) The critical yaw angle for the generation of the air cavity with specific towing speed, draught, and flare angle is discussed. The formation mechanisms of the air cavity are also elaborated in detail. Geometric characteristics of the aerated cavity as a function of yaw angles are summarized. We also found the yaw angle when the volume of the air cavity reaches the maximum.

The remainder of this paper is organized as follows. Section II provides the computational setup including governing equations, numerical methods, initial and boundary configurations, important physical parameters characterizing the cavity, and mesh convergence verification. In Sec. III, the characteristics of the aerated cavity under different yaw angles are investigated in detail, presenting the generation and evolutionary dynamics of the cavity and turbulent vortex structures as well as discussing the role of these structures in the air entrainment process. The conclusions are presented in Sec. IV.

II. COMPUTATIONAL SETUP

A. Governing equations and numerical methods

The 3D incompressible Navier-Stokes equations in Eq. (1) are solved in conservative forms:

$$\frac{\partial \rho}{\partial t} + \nabla \cdot (\rho \mathbf{u}) = 0, \tag{1a}$$

$$\frac{\partial (\rho \mathbf{u})}{\partial t} + \nabla \cdot (\rho \mathbf{u}\mathbf{u}) = -\nabla p + \nabla \cdot \boldsymbol{\tau} + \rho \mathbf{g} + \mathbf{T}_\sigma, \tag{1b}$$

where $\mathbf{u}$ is the velocity vector, and p represents the pressure. Here, $\boldsymbol{\tau}$ is the shear stress tensor, which is defined as $\boldsymbol{\tau} = \mu[\nabla \mathbf{u} + (\nabla \mathbf{u})^T]$. Also, μ and ρ are the dynamic viscosity and density, respectively, which can be obtained using the volume fraction C according to Eq. (2). Furthermore, $\mathbf{g}$ is the acceleration due to gravity, and

$$\mu = \mu_l C + \mu_a (1 - C), \tag{2a}$$

$$\rho = \rho_l C + \rho_a (1 - C), \tag{2b}$$

where the subscripts l and a represent the liquid and air phases, respectively.

In this paper, surface tension is considered, which plays an important role in the formation of small-scale structures (e.g., bubbles and droplets). Here, $\mathbf{T}_\sigma = \sigma \kappa \delta \mathbf{n}$ indicates surface tension, which is nonzero only at the location of the interface. Also, σ and κ represent the coefficient of surface tension and the local curvature of the interface, respectively. Furthermore, δ is the Dirac delta function, and $\mathbf{n}$ is the vector normal to the interface.

The governing equations are solved using the LES by applying a convolution filter to the unsteady Navier-Stokes equations. After applying the filter operation, we can obtain Eq. (3). Vortices larger than the filter width and energy carrying eddies are fully resolved, while small-scale and dissipative eddies are modeled with a subgrid scale stress model:

$$\frac{\partial \rho}{\partial t} + \nabla \cdot (\rho \bar{\mathbf{u}}) = 0, \tag{3a}$$

$$\frac{\partial \rho \bar{\boldsymbol{u}}}{\partial t} + \nabla \cdot (\rho \bar{\mathbf{u}} \bar{\mathbf{u}}) = -\nabla \bar{p} - \nabla \cdot \bar{\boldsymbol{\tau}} + \rho \mathbf{g} + \bar{\mathbf{T}}_{\sigma}, \tag{3b}$$

where $\bar{\boldsymbol{\tau}}$ is the subgrid-scale (SGS) stress tensor, which is not a closed term. In this paper, the eddy viscosity model proposed by Smagorinsky [38] is used to deal with the SGS stress.

In the present simulation, the inertial forces are dominant; thus, the subgrid stress tensor is of primary importance throughout the simulation. We follow the previous studies [39,40]. The effects of the other closed terms in the two-phase LES [41,42] are neglected. In the numerical studies of the unsteady wave breaking [43,44] and the flow around a surface-piercing structure [45,46], researchers also primarily emphasized the contributions of the stress tensor, disregarding other terms. The characteristics of the large-scale cavity and the bubble distribution are almost unaffected when ignoring the other closed terms of the variable-density LES. However, it should be noted that these closed terms may have effects on the dynamics of small bubbles (with a radius < Hinze scale 1 mm [27]) driven by surface tension, which are beyond the scope of this paper.

A brief description of the numerical methods is summarized below. The above equations are discretized based on a staggered mesh configuration, and a classical projection method [47] is employed for velocity-pressure coupling. To track the motion of interface between distinct gas and liquid accurately, a coupled level set (LS) and volume-of-fluid (VOF) method [48] with a favorable mass-preserving property is employed. In this method, the interface is reconstructed based on the VOF function, and the interface normal is computed from the LS function. The passive-scalar transport Eq. (4) is solved to obtain the motion of deformation of the interface:

$$\frac{\partial \mathrm{C}}{\partial \mathrm{t}} + \mathbf{u} \cdot (\nabla \mathrm{C}) = 0, \tag{4}$$

where $\mathrm{C} = \int_{\Omega} f(x)dx$, and $f(x)$ is the Heaviside function, which represents the interface profile.

Meanwhile, to improve the numerical robustness in simulating the high-density-ratio two-phase flows, a mass- and momentum-consistent advection method [49,50] is developed. The mass transport Eq. (1a) is solved with an upwind scheme to update the density field, and then mass fluxes $\rho\mathbf{u}$ are calculated accordingly, which is used to solve the transport of momentum. By the treatment, the spurious velocities and unphysical deformations of the interface, which are often encountered in the simulation of violent two-phase flows are eliminated, and momentum conservation of the two phases is preserved. In addition, a sharp-surface-tension-based model [51] developed from the ghost fluid method [52] is adopted to deal with flow structures driven by the surface tension force for this paper.

We apply an efficient immersed boundary (IB) method [53] to treat the IBs of the rectangular plate. The velocity boundary conditions and the velocity field adjacent to the body surface are reconstructed through interpolation. In the present IB method, the position of the body surface is identified by the signed distance function field implicitly. Thus, the velocity at the forcing points with a circular supporting domain can be obtained by an improved moving least squares method. [54] For implementation, second-order interpolation is constructed with the interpolation stencils based on the circular support domain.

In this paper, a block-structured adaptive mesh refinement (BAMR) strategy [55–57] is adopted to resolve small-scale structures with local refinement, which can significantly reduce the computational cost, allowing an efficient representation of multiscale processes. In the BAMR method, the refinement criterion is defined to ensure only the crucial regions (e.g., the flat plate, interface, and high gradient field) are covered by the fine resolution, and the grid resolution will be dynamically refined or derefined depending on the position of the interface and body surface. The whole domain is covered with blocks of various sizes, and blocks are taken as the basic manipulation units indexed

TABLE I. Computational parameters (refinement level, mesh grid resolutions, yaw angles, towing speed, etc.) used in the present simulation.

Refinement level	Mesh resolution Δ_h (mm)	Yaw angle α_E (deg)	Towing speed $U\,(\mathrm{m\,s^{-1}})$	Draught Froude number F_D
2-5	$\Delta x = \Delta y = \Delta z = 8$	45	1.75	1.25
2-6	$\Delta x = \Delta y = \Delta z = 4$	45	1.75	1.25
2-7	$\Delta x = \Delta y = \Delta z = 2$	10 20 25 30 35 40 45 50	1.75	1.25

by octree (3D) data structures with the identical logical configuration. Each block is filled with uniform Cartesian mesh, and thus, high-order interpolation schemes (e.g., WENO [58]) can be implemented without additional difficulty.

B. Initial and boundary conditions, main parameters

The numerical configuration is shown in Fig. 2, which is based on the experiments conducted in the towing tank of the Ecole Centrale de Nantes (France) by Noblesse *et al.* [36]. The simulations are conducted in a 3D computational domain, with $[-0.5\ \mathrm{m},\ 1.3\ \mathrm{m}]$, $[-0.3\ \mathrm{m},\ 1.5\ \mathrm{m}]$, and $[-0.8\ \mathrm{m},\ 1.0\ \mathrm{m}]$ in the x (inlet flow direction), y (spanwise direction), and z directions. The computational domain is large enough to capture typical flow structures in the OWB and RC regions. A rectangular flat is immersed at a draught D and speed U. The principal geometric parameters of the rectangular plate are given as follows: length $l = 0.782$ m, height $h = 0.5$ m, and draught $D = 0.2$ m. Here, $l' = \cos\alpha_E\, l$ is the length of l projected onto the x-z plane.

In the cases considered here, a constant flare angle (angle between the plate and the vertical axis) is $\gamma = 10^\circ$ and a series of yaw angles α_E (angle between the plate and inlet flow direction) are summarized in Table I. In streamwise direction, the uniform upstream velocity is $U = 1.75$ m/s, which is prescribed on the inlet plane $(-x)$, and mass conserving outflow condition is applied on the right outlet plane $(+x)$. The draught Froude number $F_D = U/\sqrt{gD}$ is used to characterize the current problem, corresponding to the Reynolds number $\mathrm{Re} = Ul/\nu_l = 3.5 \times 10^4$. Unless otherwise indicated, all length and time scales are normalized by the draught $D(0.2\ \mathrm{m})$ and the simulation time $T(2\ \mathrm{s})$, respectively.

The time-averaged free surface profile for the case of $\alpha_E = 45^\circ$ as the flow field develops to a statistically stable state is shown in Fig. 3. In this paper, the crucial parameters characterizing the aerated RC are defined as follows: L represents the length of the aerated RC, defined by the distance between the plunging and breaking points [Fig. 3(a)]. The definition of these two key points is shown in Fig. 4(a). Here, B and H are the maximum width and height of the cavity projected on the x-y and x-z planes, respectively. Also, V is the volume of the cavity. The area of the maximum cross-section of the cavity A is also considered [Fig. 3(b)]. These key parameters are used to characterize the air cavity in Sec. III.

C. Mesh convergence verification

The development of the air cavity depends on many factors; only the effects of yaw angles are investigated in this paper. Simulations are performed with eight yaw angles: $\alpha_E = 10^\circ,\ 20^\circ, 25^\circ, 30^\circ, 35^\circ, 40^\circ, 45^\circ$, and 50°, and with the towing speed $U = 1.75$ m/s (corresponding to $F_D = 1.25$), as summarized in Table I. Three types of mesh resolutions ($\Delta_h = 8$, 4, and 2 mm) for the yaw angle $\alpha_E = 45^\circ$ are considered to perform the mesh convergence study. Up to 80 million meshes are employed to discretize the 3D computational domain, particularly for relatively large yaw angles.

It is usually difficult to perform the grid convergence study for unsteady and turbulent two-phase flows owing to the transient fluid dynamics of the breaking wave. The numerical results (on three

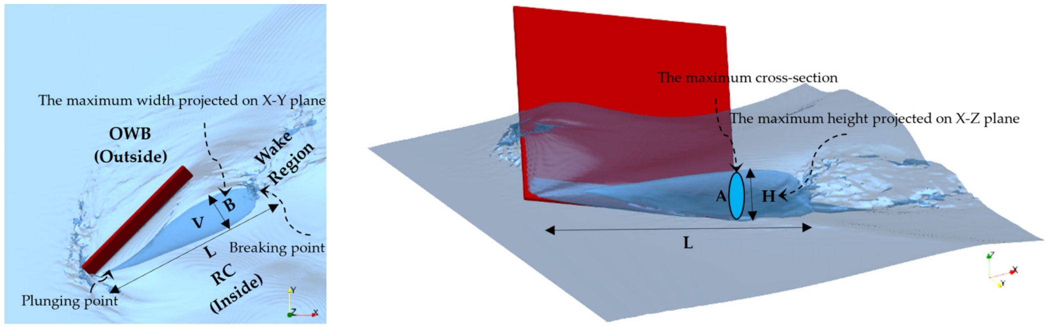

(a)

(b)

FIG. 3. Time-averaged free surface for the case $\alpha_E = 45°$. The crucial parameters characterizing the aerated rotation cavity (RC) are marked on the figures. L and V are the length and volume of the aerated RC. B and H are the maximum width and height of the cavity projected on the x-y and x-z planes, respectively. A is the area of the maximum cross-section of the cavity. (a) Top view. (b) Bottom view.

sets of meshes) for the air cavity shapes in the crossing section of $X/D = 2.5$ are presented in Fig. 5(a). Apparently, the coarse grids are not sufficient to resolve the thin liquid sheet of the air cavity. Since the overall profiles of the air cavity for the 2-6 and 2-7 mesh refinement levels are similar, we can expect the overall flow features of the air cavity can be well captured with the 2-6 refinement level (medium mesh). However, for better resolution of the bubbles, the results computed on the finest grid (2-7 refinement level) are used for the analysis. Figure 5(b) shows the time-averaged bubble size distribution $N(r)$ in the wake region for the three grid sizes, and all three bubble size distributions follow a power law $N(r) \propto r^{-10/3}$, consistent with experimental studies [25,26], which are independent of the mesh resolution. Therefore, the bubble size distribution in this paper is not affected by the grid resolution we used. Time evolutions of the nondimensional entrapped bubble number density (BND) n/N and volume $V/V_{\max}$ under three different refinement levels are shown in Figs. 5(c) and 5(d). The overall trends of the bubble density and entrapped volume for the fine and medium grids are consistent, which indicates the results are not affected by the grid sizes when the refinement level is 2-6 or 2-7. The results on coarse grids show more oscillation due to the insufficient resolution. Fine grids are used for the following discussions of the entrapped bubble density and volume, which can capture more details of small-scale structures.

III. CHARACTERISTICS OF THE AERATED CAVTTY

A. Generation of the aerated cavity

Figure 6 presents the instantaneous free surface near the plate at a statistically steady state under four different yaw angles, in which the free surface is identified using the isosurface of the volume function ($C = 0.5$). For all cases, the existence of the plate induces elevation difference of the free surface and ultimately results in air entrainment around the leading edge of the plate.

However, for the cases with relatively small yaw angles [$\alpha_E = 25°$, Fig. 6(a)], the entrapped air cannot formulate a semisimply connected cavity, and only a few small falling jets are found. This process is like that of spilling breakers in the study of canonical wave breaking [16,17]. For the case of a relatively larger yaw angle [$\alpha_E = 35°$, Fig. 6(b)], a thin and slender air tube is formed, and plenty of small bubbles detach from the tail of the air pocket. This process is analogous to the weak plunging breaker, which is situated between the spectrum of the plunging breaker and the spilling breaker. The large-scale and stable air cavity is developed in the cases of large yaw angles

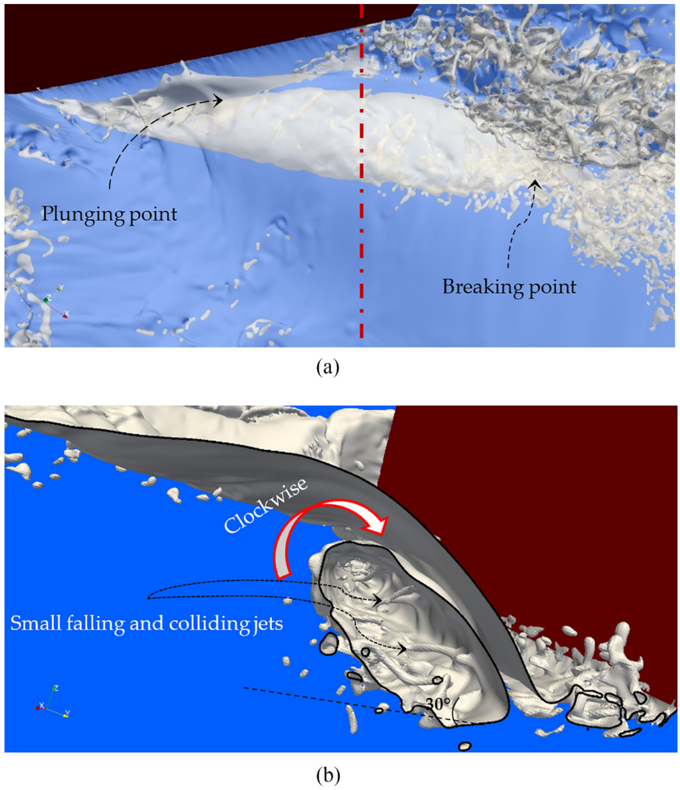

FIG. 4. (a) Close-up view of the aerated cavity, presenting the plunging point and the breaking point. The red dashed line shows the cross-section slice locations at $X/D = 2.0$. (b) Cross-section of the cavity, presenting the shape and internal small structures and indicating the rotating direction.

[$\alpha_E = 40^\circ$ and 50°, Figs. 6(c) and 6(d)], and the large air pocket contracts at the tail and breaks into a large number of bubbles with various scales, forming bubble plumes in the wake region finally.

The profiles of the air cavity on the y-z plane, $X/D = 2.0$ with different yaw angles ($\alpha_E = 10^\circ$, 20°, 30°, 35°, and 40°) are presented in Fig. 7(a), for further demonstrating the origin. Apparently, once the towing speeds are determined, the development of the air cavity mainly depends on the yaw angles. We find that the air cavity grows into stabilized structures only for appropriate yaw angles ($\alpha_E \geqslant 35^\circ$), in which stronger plunging wave breakers are induced in the RC region. A small jet is still clearly visible for the yaw angles $\alpha_E = 20^\circ$ and 25°, but it does not impact the face of the wave. For the yaw angle $\alpha_E = 30^\circ$, the jet is more energetic to impact the free surface without being isolated from the main surface, so the entrapped tube is connected with the upper wave face. For large yaw angles ($\alpha_E = 35^\circ$ and 40°), the jets from the crest of the wave intensely impact the forward face of the wave, developing into an overturning motion and falling off to form a large-scale air pocket. As shown in Fig. 7(b), vorticity is produced under the free surface due to the presence of the plate, causes velocity deficit, and influences the dynamics of the interface, which can be used to explain the generation of the air cavity under different yaw angles. The interface begins to roll up under the action of the vortex, and the vorticity strongly depends on the yaw angle. With the yaw angle increase, the blocking effect of the structure is stronger, resulting in a larger velocity deficit and forming a stronger vorticity. For small yaw angles ($\alpha_E = 20^\circ$), vorticity is weak, and only a small jet structure appears. When the yaw angle is $\alpha_E = 30^\circ$, the stronger vortex leads to an increased stretching of the interface, which tends to fall up. A significant increase is seen in the vorticity production for the case $\alpha_E = 35^\circ$, which has enough energy to distort the interface,

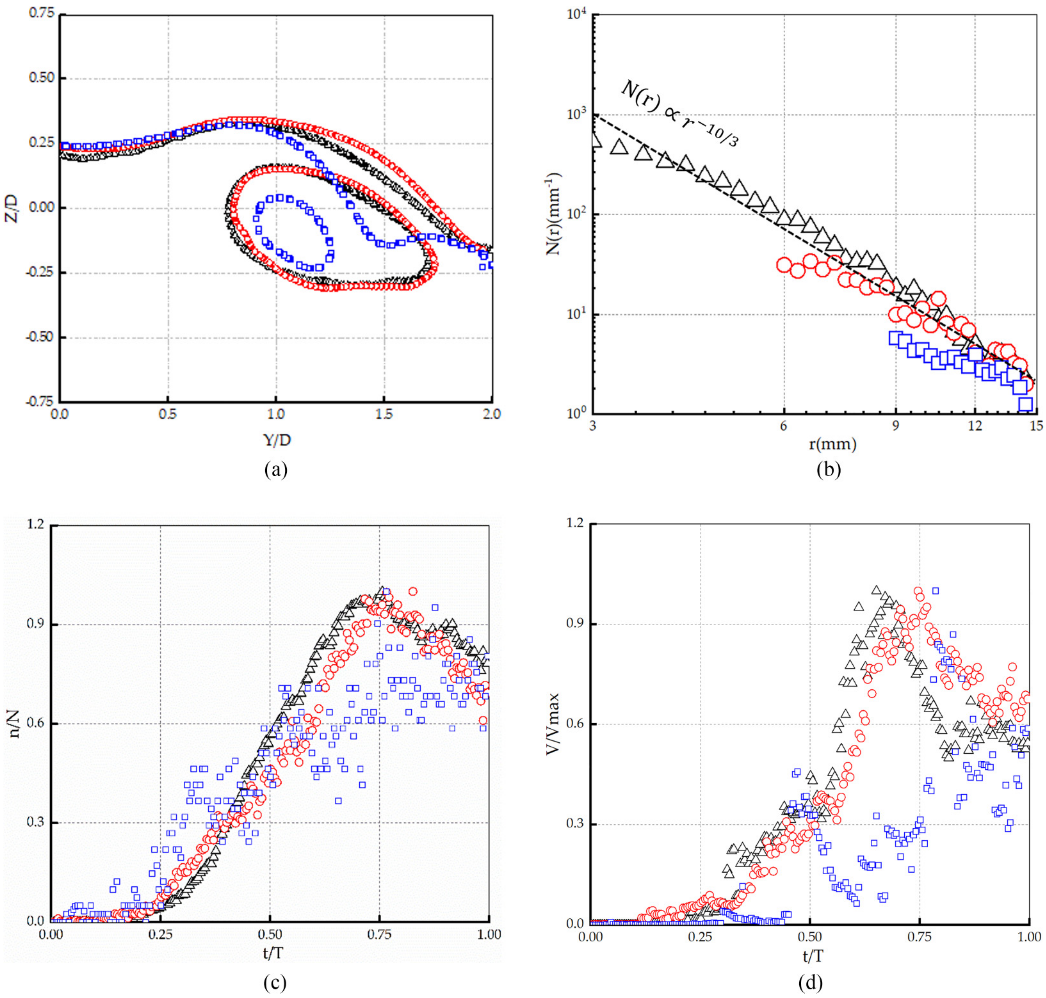

FIG. 5. Convergence study for three grid resolutions. Coarse grids (2-5, □), medium grids (2-6, O), and fine grids (2 − 7, Δ), (… …): $N(r) \propto r^{-10/3}$. (a) Wave profiles of the aerated cavity in the crossing section of $X/D = 2.5$. (b) Time-averaged size distribution $N(r)$ of bubbles in the wake region. (c) Time evolution of the nondimensional number density n/N (N is the maximum number density) of the entrapped bubbles. (d) Time evolution of the nondimensional entrapped bubble volume $V/V_{\max}$ ($V_{\max}$ is the maximum air volume).

trapping an air cavity within the vortex. Thus, for the cases $\alpha_E \geqslant 35^\circ$, the air cavity develops into a stable rotational state under strong vortices.

Figure 7(c) gives the time-averaged results of free surface, and the large-scale air cavity is clearly visible for the cases of large yaw angle ($\alpha_E \geqslant 35^\circ$). The time-averaged operation is performed when the flow is fully developed (steady-state period), and the average period is from $t = T$ to $t = 1.25T$. Figure 7(d) shows the average free surface with wave elevation, and a depressed region near the plate is observed due to the blocking effect of the structure. The region broadens as the yaw angle increases. Two continuous opposite flows are triggered by the reverse flow in the depressed region [as shown in Fig. 7(e)], and considerable topologically induced circulation takes place, which corresponds to the generation of vortices in Fig. 7(b). The size of the entrapped air cavity is closely related to the vortices. The shears from the two opposite flows are not enough to overcome the stability of the air-water interface without inducing a stabilized and continuous air cavity when the

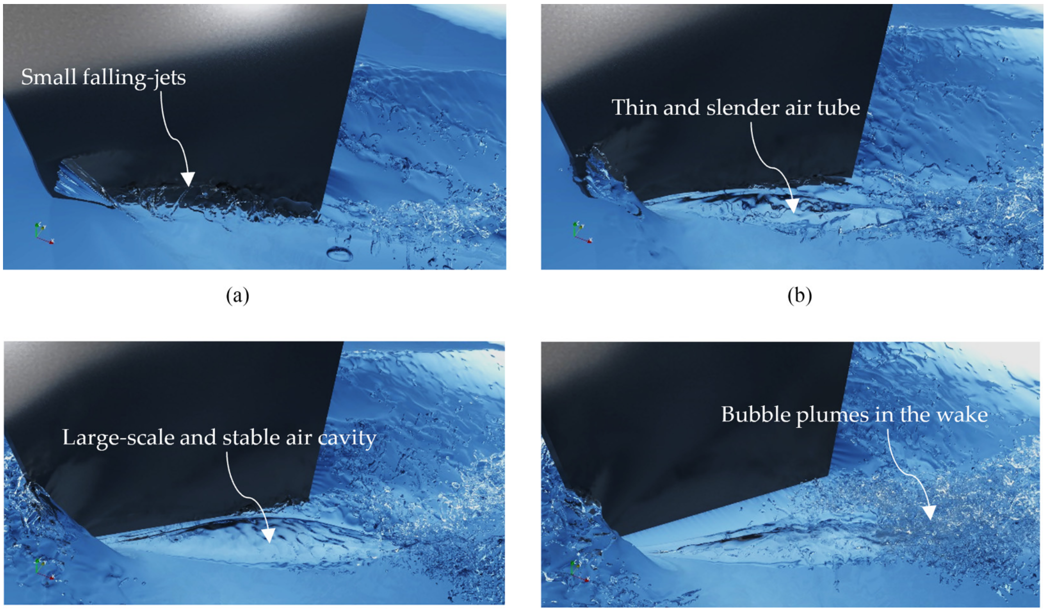

(a) (b) (c) (d)

FIG. 6. Aerated cavity structures inside of the plate [rotation cavity (RC) region, as indicated in Fig. 2(a)] at a statistically stable stage for the different yaw angles. No obvious aerated cavity is observed for the relatively small yaw angles: (a) $\alpha_E = 25^\circ$. The thin and slender air tube starts to occur at (b) $\alpha_E = 35^\circ$. A large-scale air pocket rotating inside of the plate can be found at (c) $\alpha_E = 40^\circ$ and (d) $\alpha_E = 50^\circ$.

strength of vortices is small [Fig. 7(b)]. However, strong vortices will steepen the wave breaker and force the air cavity to be more elliptical [Fig. 8(b)], resulting in a volume reduction. The case $\alpha_E = 40^\circ$ has the largest volume of entrapped air cavity with moderate vortices, which is confirmed below.

Figures 9(a) and 9(b) show spatial distribution of turbulent kinetic energy (TKE) at different streamwise locations for the cases $\alpha_E = 35^\circ$ and 50°. The Favre-averaged velocity [59] is defined as

$$\bar{\mathbf{u}} = \frac{\overline{\rho \mathbf{u}}}{\bar{\rho}}, \tag{5}$$

and the corresponding velocity fluctuation $\mathbf{u}'$ and mean TKE k are, respectively,

$$\mathbf{u}' = \mathbf{u} - \bar{\mathbf{u}}, \tag{6}$$

$$k = \tfrac{1}{2}\overline{\mathbf{u}'\mathbf{u}'}. \tag{7}$$

The bar represents the time-averaging operator here.

The statistical results of TKE show that the strong turbulence region is mainly related to the formation and breakup of the air cavity. Before the breaking of the air cavity, the TKE is mainly caused by the impact of the falling jet and splash. As the air cavity develops downstream, the TKE become larger gradually owing to the instability around the rear of the air cavity. Bubbles are generated when the trailing part of air cavity further destabilizes, which produces the highly turbulent flow, involving different physics processes, such as air entrapment, vortices interacting with the surface, and so on. The maximum TKE appears in this region. From the velocity vector field, there is a high circulation of water surrounding it as the air cavity rotates, evolving around the center of the air cavity.

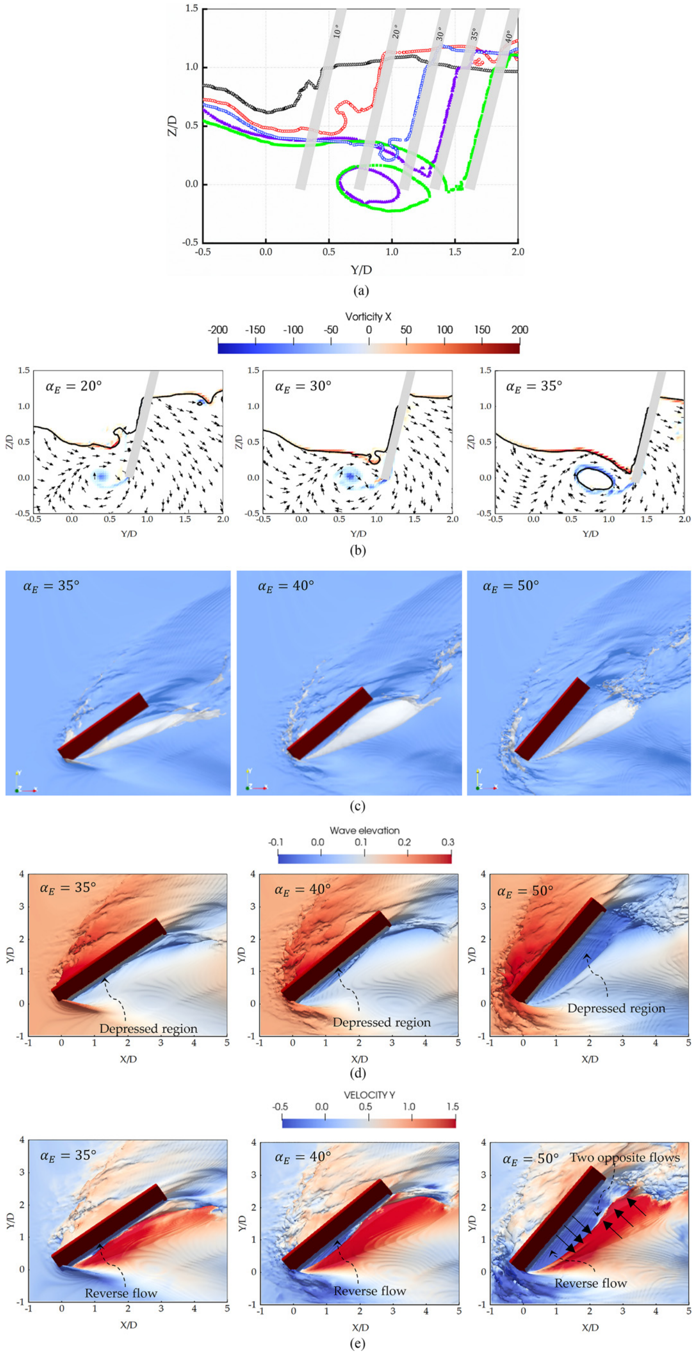

FIG. 7. (a) Air cavity profiles cut perpendicular to the x direction, at the $X/D = 2.0$ position at a stable stage for the different yaw angles, showing the generation of the rotation air cavity from small yaw angles to relatively large yaw angles (10°–40°). (△): $\alpha_E = 10°$, O: $\alpha_E = 20°$, (□): $\alpha_E = 30°$, (▲): $\alpha_E = 35°$, and (■): $\alpha_E = 40°$. The gray box represents the projection of the plate on the y-z plane. (b) Transverse cuts of average planar velocity and vorticity fields. (c) Time-averaged results of the free surface at large yaw angle ($\alpha_E \geqslant 35°$). (d) Time-averaged results of a free surface indicating wave elevation. (e) Time-averaged results of a free surface colored by velocity in the y direction.

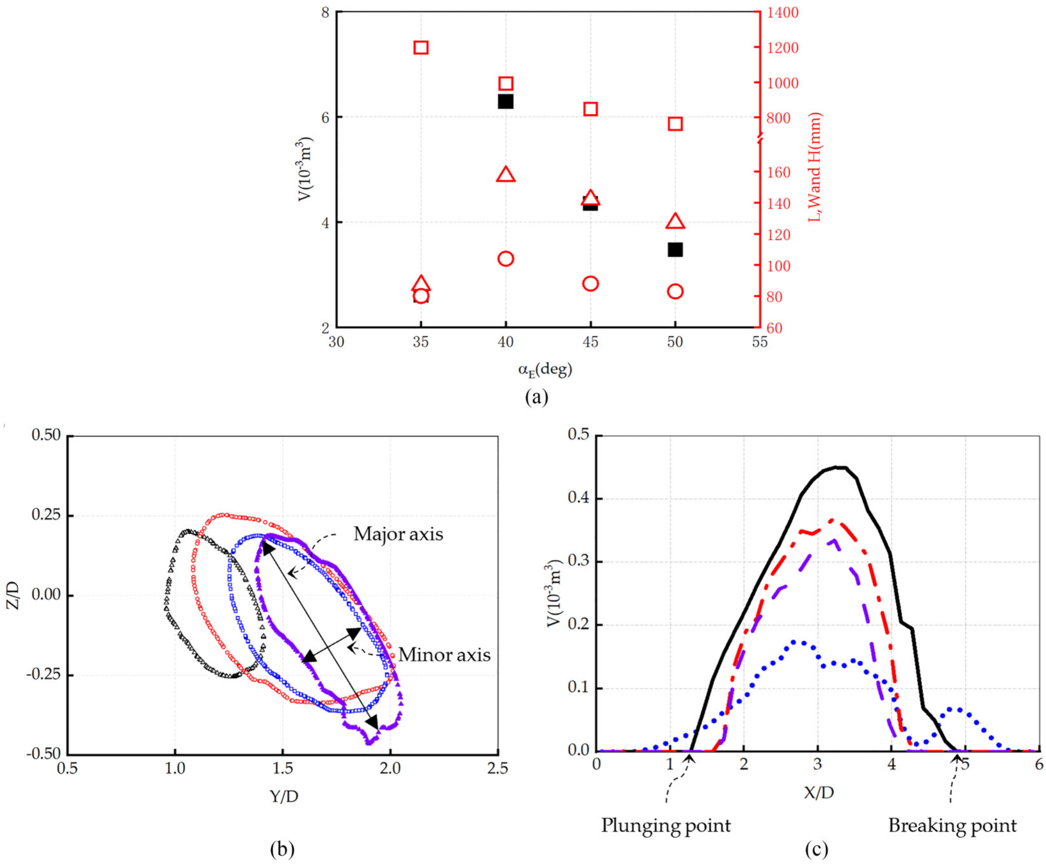

FIG. 8. Pictures showing the geometrical parameters, cross-sections, and the entrapped volume of the aerated cavity for different yaw angles based on the time-average results. (a) Characteristic parameters (volume, length, width, and height) of the cavity. (■): volume, (□): length, (△): width, and (O): height. (b) The cross-section of the air cavity cut perpendicular to the x direction. (△): $\alpha_E = 35^\circ$, (O): $\alpha_E = 40^\circ$, (□): $\alpha_E = 45^\circ$, and (▲): $\alpha_E = 50^\circ$. (c) The entrained air volume along the streamwise direction per unit distance. (……): $\alpha_E = 35^\circ$, (—): $\alpha_E = 40^\circ$, (_•_): $\alpha_E = 45^\circ$, and (- - -): $\alpha_E = 50^\circ$.

B. Temporal and spatial evolution of the aerated cavity

The whole formation process of the aerated cavity, including the generation of the overturning jet, entering the water, rolling over, and collapsing at the tail, is presented in Fig. 10 for the case $\alpha_E = 45^\circ$. More details of the temporal and spatial evolution are shown in the Supplemental Material video [60]. The process from the beginning of air pocket generation to a statistically stable stage is demonstrated as follows. At the initial stage [$t/T = 0.25$, Fig. 10(a)], the interface begins to roll and curl, and a slender air tube is ingested into the liquid bulk at the leading portion, interacting with the surrounding free surface, with some minor shedding of bubbles appearing off. At $t/T = 0.35$ [Fig. 10(b)], the initial air tube continues to rotate backward, entrapping more air, an initial air pocket forms at the middle portion of the plate, and the tail begins to be deformed. When $t/T = 0.5$ [Fig. 10(c)], the air pocket extends to the outer edge of the plate, and the trailing part of air cavity further destabilizes, breaking into many bubbles. With the development of the air cavity, the free surface becomes completely chaotic. The tail of the air cavity is destroyed, leaving a dense bubble plume. Later, at $t/T = 1.0$ [Fig. 10(d)], the air cavity reaches a statistically stable stage finally, with

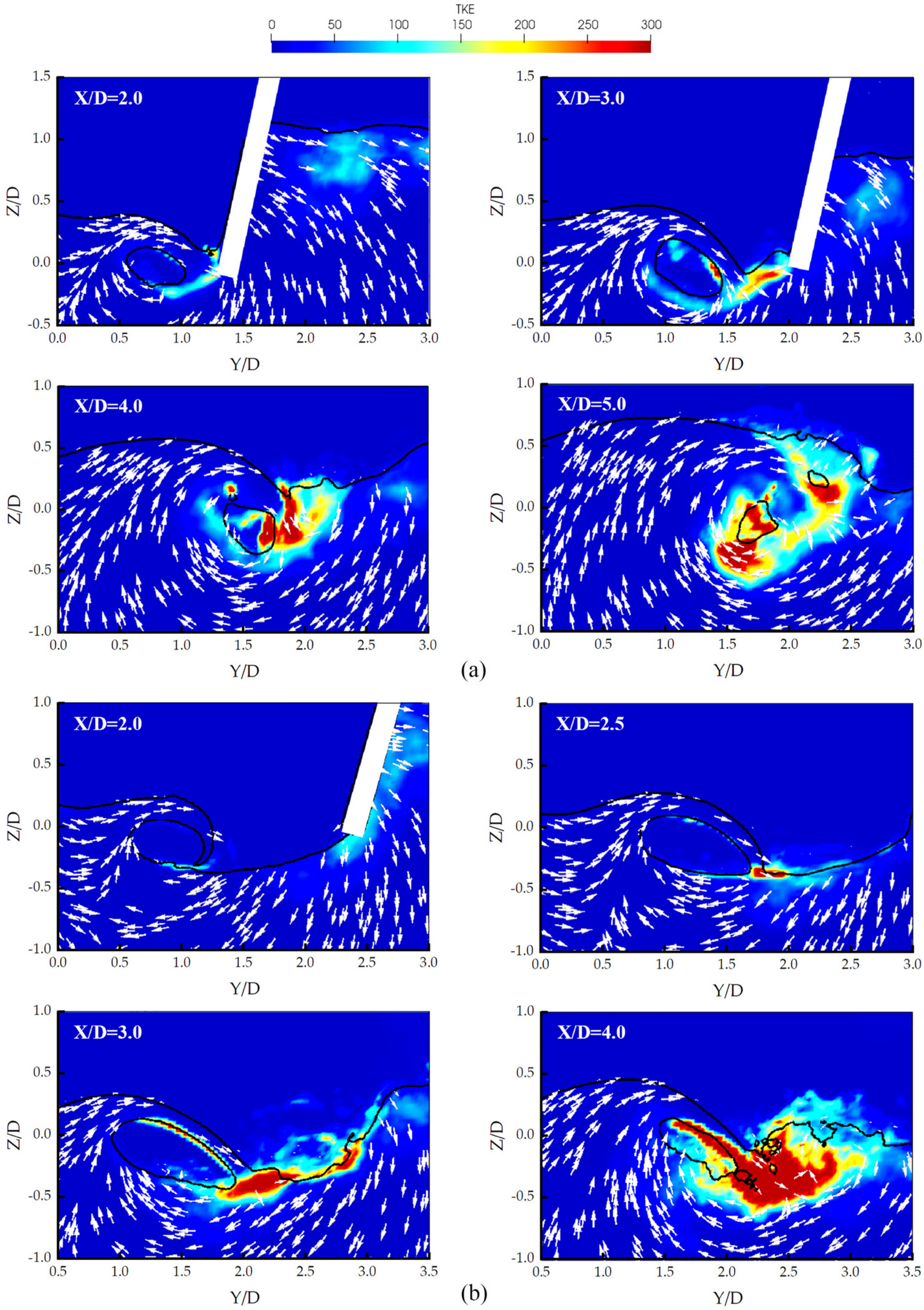

FIG. 9. Spatial distribution of turbulent kinetic energy at different streamwise locations. (a) $\alpha_E = 35^\circ$ and (b) $\alpha_E = 50^\circ$.

the main stem rotating at a certain speed and a very large array of bubbles pinching off from the end.

A close-up view of the aerated cavity is shown in Fig. 4(a), giving two crucial positions which are related to the formation and evolution of the air cavity. One is the plunging point where the

(a)

(b)

(c)

(d)

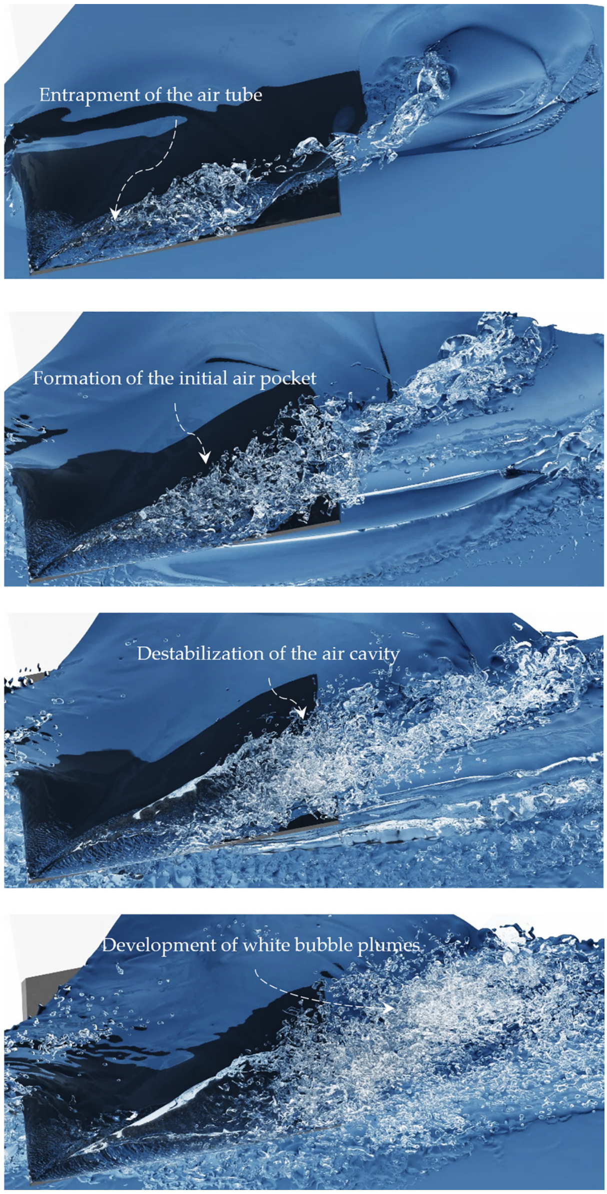

FIG. 10. Sequence of snapshots presenting the whole formation process of the aerated cavity, from the beginning of air pocket generation to the statistically stable stage. (a) Entrainment of a small air tube $t/T = 0.2$. (b) Formation of the initial air pocket $t/T = 0.35$. (c) Collapse of the tail of the air cavity and accumulation of massive bubbles $t/T = 0.5$. (d) Reaching a statistically stable stage $t/T = 1$. See Supplemental Material [60] for the detailed temporal and spatial evolution process of the aerated cavity.

jet impacts the free surface. Another is the breaking point where the air cavity begins to collapse, and many bubbles appear after this point. Figure 4(b) is the profile of the air cavity at the red line position [$X/D = 2.0$, Fig. 4(a)], which clearly demonstrates the cross-section of the air cavity. The cavity shape is not truly circular but more closely approximates an elliptical shape, rotating at an angle of $\sim 30^\circ$ to the horizontal line. The inside of the air cavity is not hollow, and there are many small-scale structures, such as falling and colliding jets, inside the air cavity. These structures are

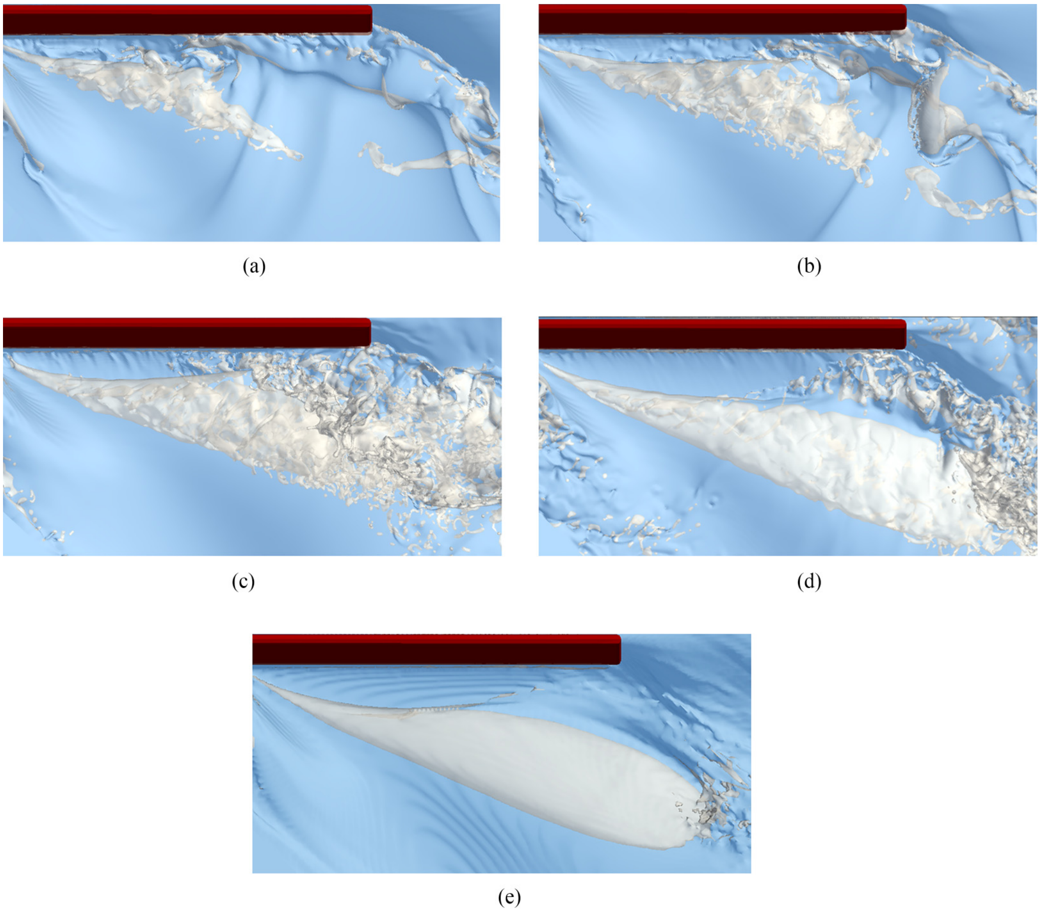

FIG.11. Evolution of the air cavity shape over time (a)–(d) for case $\alpha_E = 45^\circ$. (e) The time-averaged result of the air cavity. (a) $t/T = 0.18$, (b) $t/T = 0.25$, (c) $t/T = 0.38$, and (d) $t/T = 0.75$.

very small compared with the main air pocket, and their average diameter is only 0.002 m. The reasons for the generation of these jets may be inertia resulting from the rotation of the air cavity. This, we can judge the rotating direction with these jets. As shown by the red arrow, the rotating direction of the main air pocket is clockwise from the $-x$ direction.

Figures 11(a)–11(d) show the evolution of the air cavity shape over time. In the early stage ($t/T = 0.18$), a small amount of air is entrained, forming an initial pocket that appears long and narrow. As the entrainment process develops, the air cavity gradually evolves into an approximately conical shape at $t/T = 0.25$. The tail of the air cavity breaks due to the flow instability ($t/T = 0.38$). The air cavity finally reaches a stable state with a conical shape ($t/T = 0.75$). Figure 11(e) shows the time-averaged profile of the air cavity for $\alpha_E = 45^\circ$ and $F_D = 1.25$.

In this section, detailed quantitative descriptions and general trends of the aerated cavity are presented. Certain critical parameters of the aerated cavity defined in Fig. 3 are measured to characterize the cavity. Table II summarizes the characteristic parameters of the aerated cavity, as a function of yaw angles based on the time-averaged results.

Figure 8 presents descriptions of the air cavity under different yaw angles, including the main geometrical characteristics (volume, length, width, and height), the wave profile, and the entrained air volume along the streamwise direction per unit distance. As shown in Fig. 8(a), different from what we expected, the volume of the entrapped air cavity does not increase with the intensity of

TABLE II. Characteristic parameters (volume, length, width, etc.) of the aerated cavity as a function of yaw angles.

Yaw angle α_E (deg)	Volume V (10^{-3} m^3)	Length L (mm)	Width B (mm)	Height H (mm)	Area A (10^{-3} m^2)
35	2.607	1145	87	80	5.856
40	6.286	992	157	104	14.213
45	4.350	848	142	88	9.991
50	3.471	762	127	83	8.673

the rotation. We find that the total measured volume of the air cavity depends on its length and the area of the cross-section. The case of $\alpha_E = 40^\circ$ shows the air cavity with the largest volume because of its largest cross-sectional area and relatively long length. The length of the air cavity shortens with the increase of the yaw angle. The trend of the width and height of the air cavity is like that of the length for $\alpha_E > 40^\circ$ cases. Figure 8(b) presents the areas (A) of the cross-section, which have been summarized in Table II. As the yaw angle increases, the rotation of the air cavity becomes more violent. Thus, the profile gains a larger penetration depth, and the ratio of the major axis to the minor axis is larger, which results in a more elliptical section. Figure 8(c) shows the spatial evolution of the entrapped volume along the streamwise direction, and the integral under the curve is consistent with the volume of air cavity. The figure provides insight into the cross-sectional trend of the air cavity along the x direction to some extent, showing an initial increase in size followed by a subsequent decrease. The points at which the air cavity volume $V = 0$ correspond to the plunging and breaking points [Fig. 4(a)], respectively. For small yaw angles ($\alpha_E = 35^\circ$ and 40°), the plunging point is more forward, and the breaking point is further back, indicating a long and slender air cavity. The maximum cross-section appears at the position $X/D \approx 3.0$ for each case.

Having discussed the characteristics of the air cavity, we now turn to quantifying the entrained bubble properties in the wake based on the bubble-droplet detection program [4]. As shown in Fig. 12, the time-averaged (over the stable state with $1.0 \leqslant t/T \leqslant 1.2$) free surface of the aerated cavity and the spatial distribution of bubbles in the wake under different yaw angles are presented for comparison. The left column shows the top view of the whole computational domain, which presents the overall distribution of the air cavity and bubbles in the wake region. It is noted that the bubbles in the OWB region [as indicated in Fig. 2(a)] are not shown due to the focus of this paper. To show the distribution of the bubbles behind the air cavity, a side view of the wake region is displayed in the right column. For the time-averaged results of the air cavity, we can observe that the overall length of the air cavity declines with the increase of the yaw angles, and the breaking point moves forward, which is consistent with Fig. 8(c). For the distribution of the bubbles in the wake region, the spread range of the bubble spatial distribution is broader with the increase of the yaw angles (the left column of Fig. 12). In addition, a few bubbles appear at the edge, except in the case of $\alpha_E = 35^\circ$, owing to the weak impact in the RC region [as indicated in Fig. 2(a)].

The large-scale air pocket (appears in leading edge of the plate) and the associated bubbles generated by it contribute much more air entrainment in the wake than that of the bow wave breaking. As shown in Table III, the total volume (V_{total}) of the entrapped bubbles is divided into parts, in the OWB (V_{owb}) and wake (V_{wake}) regions. The volume of the air cavity (V_{cavity}) is obtained separately to evaluate the contribution in the air entrainment. We find that the volume of the air cavity is much more than the volume of the entrapped bubbles (e.g., $V_{\text{cavity}} \approx 10V_{\text{total}}$ for the case $\alpha_E = 40^\circ$). Meanwhile, the volume of bubbles generated by the breakup of the air cavity in the wake accounts for most of the total volume of bubbles (e.g., $V_{\text{wake}} \approx 0.64V_{\text{total}}$ for the case $\alpha_E = 45^\circ$).

The volume and BND of the entrapped bubbles in wake regions are, as shown in Fig. 13, as a function of time t/T for different yaw angles. At the early stage, almost no air is entrapped until

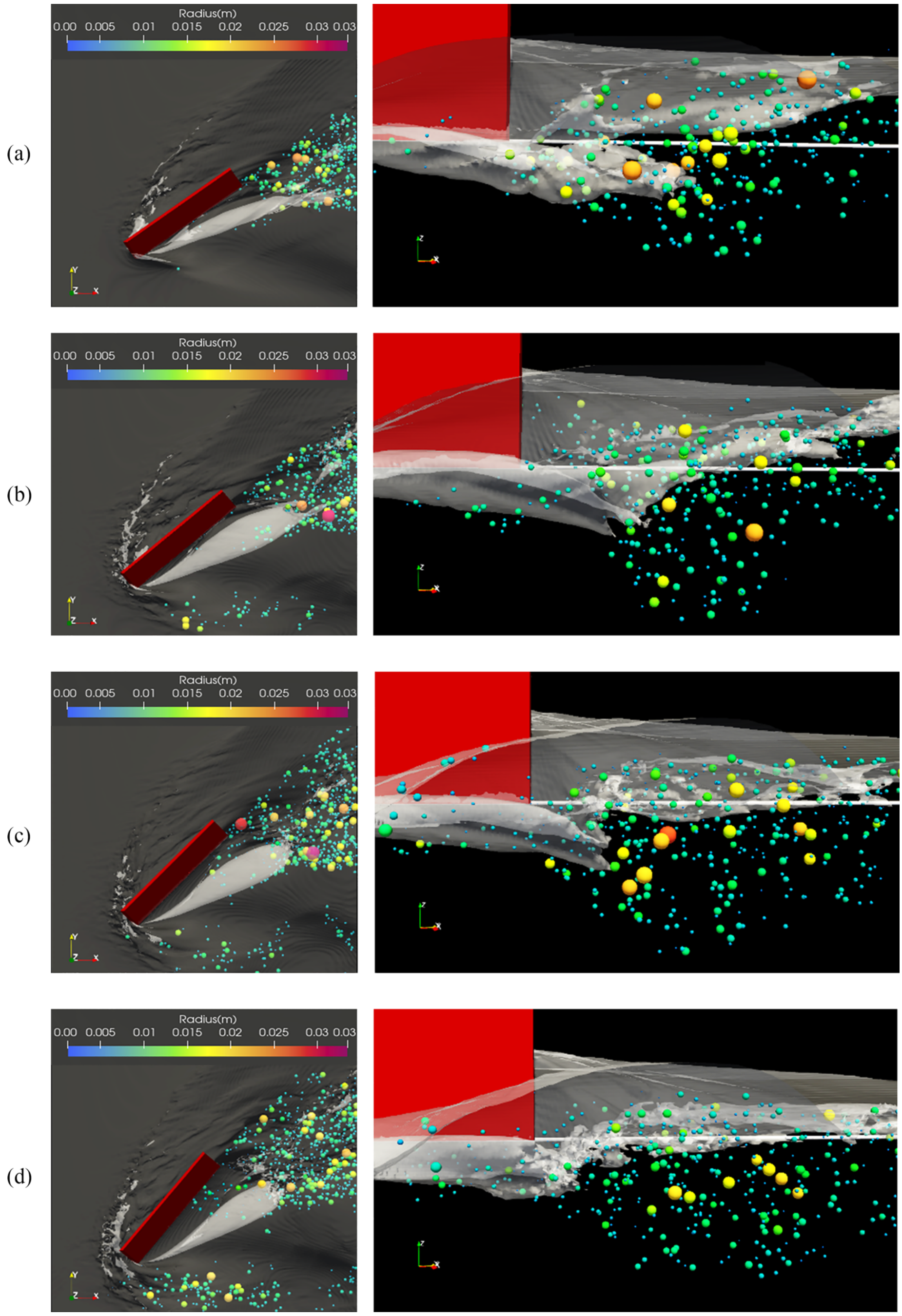

FIG. 12. Snapshots presenting the time-averaged free surface and distribution of bubbles underwater in the wake for the different yaw angles. Bubbles are represented with an equivalent spherical radius. Bubbles in the overturning wave breaking (OWB) region [as indicated in Fig. 2(a)] are not shown in the figure due to the focus of this paper. The white lines in the right column are horizontal line $z = 0$ m. The left-hand column is top view of the whole computational domain (x-y plane), and the right-hand column is side view of the wake region (x-z plane). (a) $\alpha_E = 35^\circ$, (b) $\alpha_E = 40^\circ$, (c) $\alpha_E = 45^\circ$, and (d) $\alpha_E = 50^\circ$.

TABLE III. The volume of each part and its proportion as a function of yaw angles when the flow field is fully developed.

Yaw angle α_E (deg)	V_{cavity} (10^{-3} m^3)	V_{wake} (10^{-3} m^3)	V_{owb} (10^{-3} m^3)	V_{total} (10^{-3} m^3)
35	2.607	0.119 (31.2%)	0.263 (68.8%)	0.382
40	6.286	0.341 (53.0%)	0.302 (47.0%)	0.643
45	4.350	0.668 (63.6%)	0.383 (36.4%)	1.051
50	3.471	0.696 (61.6%)	0.433 (38.4%)	1.129

$t/T = 0.20$ for all cases. From $t/T = 0.25$ to 0.75, the entrapped air volume experiences a rapid increase and reaches the peak, at which many bubbles are generated due to the breakup of the air cavity, particularly for larger yaw angles. For the case $\alpha_E = 50^\circ$, the peak time shows a slight delay, which is correlated with the more intense breakup at the tail of the air cavity. For the later stage ($t/T > 0.8$), some larger bubbles rise back to the interface and burst under the buoyancy effect, which results in the decay of the air entrainment. For the BND in Fig. 13(b), it increases with the increase of yaw angles, and most bubbles are generated in the later stages ($t/T > 0.7$). We notice that the BND of case $\alpha_E = 45^\circ$ is less than that of case $\alpha_E = 50^\circ$ at the last moment, different from the trend of the entrapped air volume, suggesting that the rotational process is more intense and produces more small bubbles for the larger angles. This phenomenon can be confirmed in Fig. 14.

Figure 14(a) shows the time-averaged bubble size distribution $N(r, t)$ over the time $t/T \in [0.8, 1.0]$ for different yaw angles, and each case follows the power-law scaling $N(r, t) \propto r^{-10/3}$. Figures 14(b)–14(e) give the contours resulting from the bubble size distribution over time and radius. The size of most bubbles is mainly concentrated in the range of 3–6 mm. Before $t/T = 0.2$, there are almost no bubbles in each case because the air cavity has not broken, which is consistent with the Fig. 13. An array of relatively small-scale bubbles (<5 mm) is generated owing to the destabilization of the air cavity at $t/T = 0.2$. Bubbles <4 mm begin to appear in large numbers owing to the breakup of large bubbles and the air cavity when it reaches the rear of the plate at later times ($t/T > 0.5$) [see Fig. 10(c)]. Two processes control the production of the relatively small bubbles ($r < 4$ mm) and the resulting size distribution: (i) the breakup of the air cavity, leading to the initial distribution, and (ii) the interaction between the entrapped bubbles in the later stage. The number of smaller bubbles ~3.5 mm is closely related to the yaw angles, suggesting that the

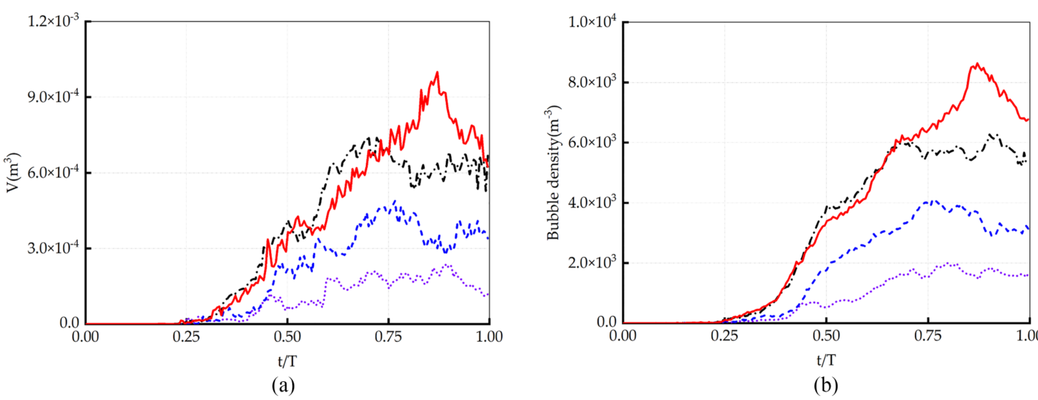

FIG. 13. Time evolution of the volume and the number density of the entrapped bubbles in the wake region for the different yaw angles. (......): $\alpha_E = 35^\circ$, (- - -): $\alpha_E = 40^\circ$, (—•—): $\alpha_E = 45^\circ$, and (—): $\alpha_E = 50^\circ$. (a) Volume (m^3). (b) Bubble density (m^{-3}).

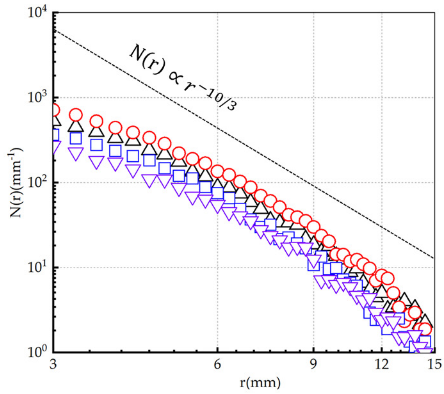

(a)

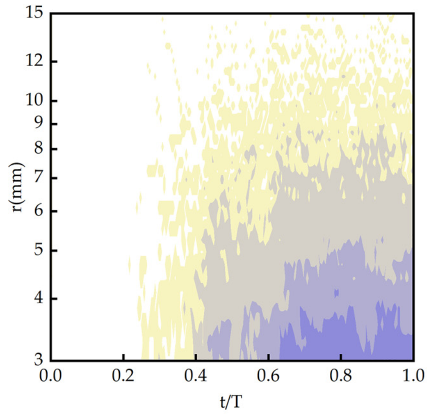

(b)

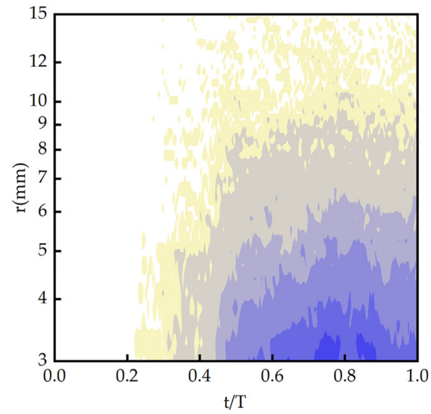

(c)

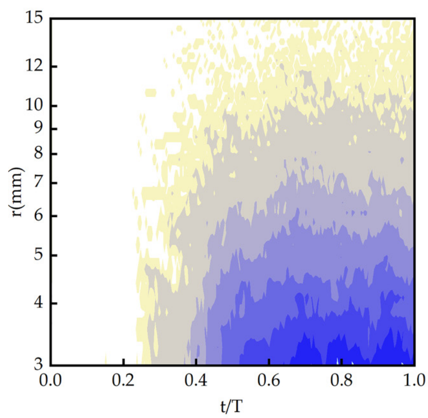

(d)

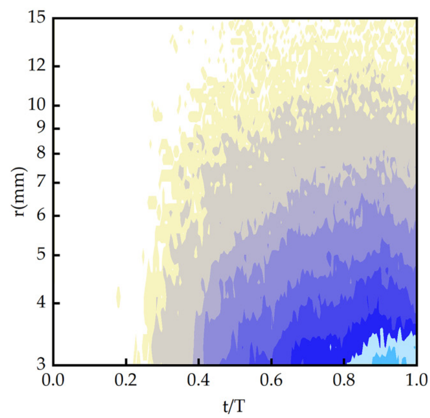

(e)

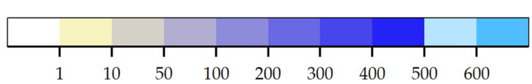

FIG. 14. (a) Time-averaged bubble size distribution of different yaw angles. (- - -): $N(r) \propto r^{-10/3}$, (▽): $\alpha_E = 35^\circ$, (□): $\alpha_E = 40^\circ$, (△): $\alpha_E = 45^\circ$, and (O): $\alpha_E = 50^\circ$. Contours of bubble size distribution $N(r, t)$ (the number of bubbles per 0.3 mm radius in this paper) over time and radius for different yaw angles. (b) $\alpha_E = 35^\circ$, (c) $\alpha_E = 40^\circ$, (d) $\alpha_E = 45^\circ$, and (e) $\alpha_E = 50^\circ$.

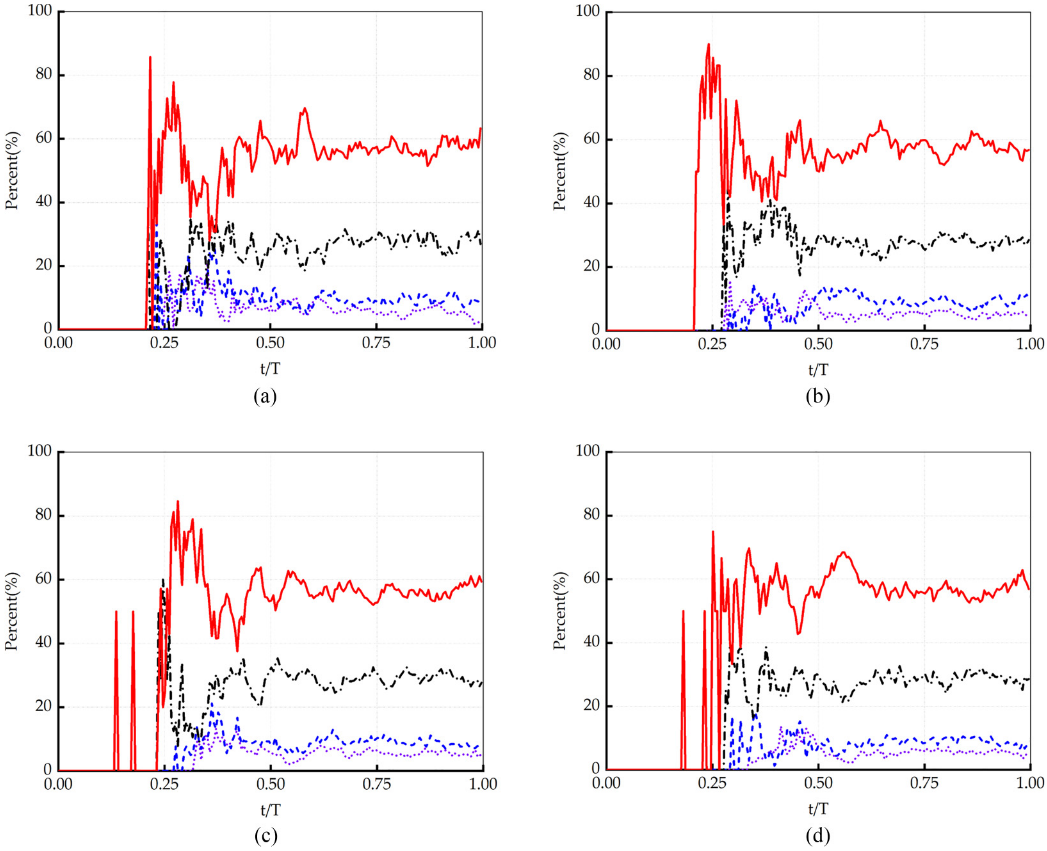

FIG. 15. Distributions of bubbles in different size ranges over time for different yaw angles. (.....): $r \geqslant 8$ mm, (- - -): 6 mm $\leqslant r < 8$ mm, (—•—): 4 mm $\leqslant r < 6$ mm, and (—): $r < 4$ mm. (a) $\alpha_E = 35^\circ$, (b) $\alpha_E = 40^\circ$, (c) $\alpha_E = 45^\circ$, and (d) $\alpha_E = 50^\circ$.

air cavity is more energetic to produce smaller bubbles for the larger yaw angles. We notice that there are more bubbles ($r < 3.5$ mm) for the case $\alpha_E = 50^\circ$ than that of the case $\alpha_E = 40^\circ$ at the stable stage; that agrees with Fig. 13. Small numbers of large bubbles (>10 mm) appear randomly (scattered on the plots) due to bubble coalescence and the breaking up of the free surface throughout the breaking process ($t/T > 0.4$).

Distributions of bubbles in size ranges for different yaw angles are presented in Fig. 15. The distribution is not sensitive to the yaw angle, and the total count is dominated by small bubbles <4 mm, occupying 60% for each case. Large-scale bubbles ($r > 6$ mm) only occupy a small part, ~15%. In all ranges, bubbles reach a stable state after $t/T = 0.5$, corresponding to the moment when the air cavity extends to the tail of the plate.

To investigate and compare the spatial distribution of air entrainment for all cases in the bubbly wake, an equivalent of the experimentally measured void fraction (Rojas and Loewen) [61] can be computed by averaging the phase function $C(x, y, z)$ over the streamwise x direction in the wake bubble region from the 3D data. The expression is given as

$$\alpha(y, z) = \frac{1}{L} \int_a^b C(x, y, z) dx, \tag{8}$$

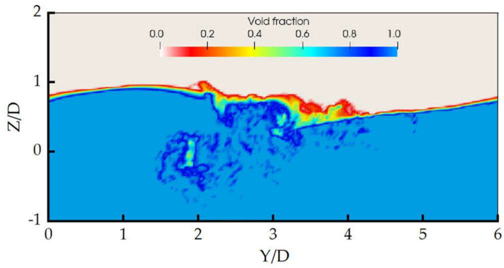

(a)

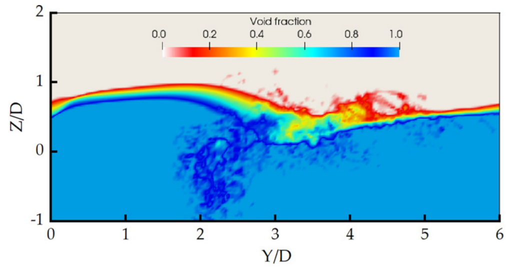

(b)

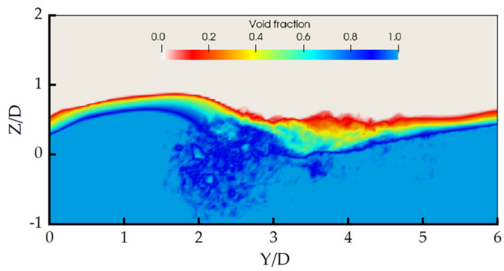

(c)

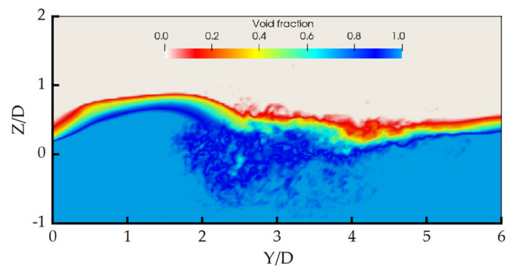

(d)

FIG. 16. Streamwise-integrated void fraction $\alpha(y, z, t) = \frac{1}{L}\int_a^b C(x, y, z)dx$, from the three-dimensional (3D) data for the different cases in the bubbly wake region at $t/T = 1.0$, a is the breaking point of the air cavity, $b = 6.5D$ is the endpoint of the computational domain, and L is the length of the wake region over the streamwise x direction. (a) $\alpha_E = 35^\circ$, $a = 5.475D, X \in [5.475D, 6.5D]$, $L = 1.025D$. (b) $\alpha_E = 40^\circ$, $a = 4.875D, X \in [4.875D, 6.5D]$, $L = 1.625D$. (c) $\alpha_E = 45^\circ$, $a = 4.275D, X \in [4.275D, 6.5D]$, $L = 2.225D$. (d) $\alpha_E = 50^\circ$, $a = 4.125D, X \in [4.125D, 6.5D]$, $L = 2.375D$.

where a is the breaking point of the air cavity, b is the endpoint of the computational domain, and $L = b - a$ is the length of the wake region over the streamwise x direction. The values of these quantities can be obtained according to Fig. 8.

Figure 16 shows the streamwise-integrated void fraction (volume of air per unit distance) for different cases in the bubbly wake region at the stable stage. Bubble plumes are formed beneath the free surface during the air entrainment process, and high void fraction areas are visible. The main concern is the penetration depth of these bubble clouds. For the case $\alpha_E = 35^\circ$, relatively shallow bubble clouds are formed beneath the surface, and the bubble clouds show scattered properties, which agrees with the Fig. 12. For larger yaw angles ($\alpha_E = 40^\circ, 45^\circ$, and 50°). These bubble plumes appear very dense and are driven into the water, reaching a maximum penetration depth. Then the bubble clouds spread horizontally, and some bubbles rise back to the surface to burst. In addition, the bubble clouds are transported further in the spanwise direction (y direction) with the increase of the yaw angle.

C. Turbulent vortex structures around the aerated cavity

In this paper, the rotating air cavity gives rise to two phenomena. On one hand, a large-scale air pocket forms, generates a mixing of air and water, and creates strong dynamics, as discussed above. On the other hand, following the formation of the air cavity, large-scale vortex structures are observed when the air cavity rotates. The 3D vortex structures below the free surface at the stable stage are identified using the Q-criterion (Q is the second invariant of the velocity gradient tension, and the Q-criterion represents the balance between the rotation and strain rates), which are shown in Fig. 17 for the case $\alpha_E = 50^\circ$. To investigate the coherent structures in more detail and the effects of vortices on the air entrainment process, the vortex structures are displayed in

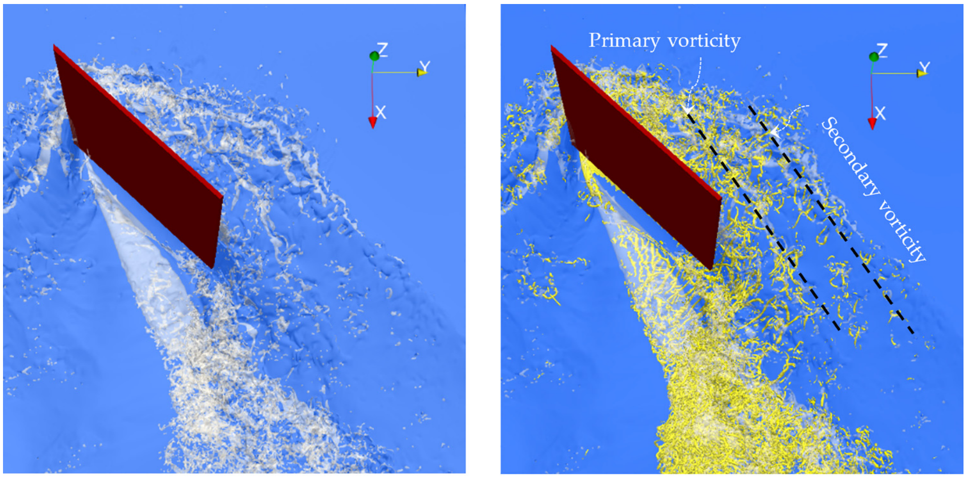

(a) (b)

FIG. 17. Three-dimensional (3D) instantaneous vortex structures in the water phase for the case $\alpha_E = 50^\circ$ at a statistically stable stage $t/T = 1$. (a) Free surface with the isosurface of the phase function $C = 0.5$ (in white). (b) Vortex structures underwater with Q-criterion (in yellow) along with the interface.

Fig. 17 with the free surface topography. Figure 17(a) shows the free surface, and underwater vortex structures are presented in Fig. 17(b) for comparison. It is noted that Q isosurfaces are only plotted for the water phase. The stabilization of the free surface is maintained by surface tension and gravity. From Fig. 17(b), it is evident that the generation of vortex structures is mainly distributed in the breaking zone, which suggests that the entrainment process could happen when vortices resulting from rotation of the air cavity are strong enough to overcome the stabilization of the free surface. Meanwhile, the vortices also interact with the free surface, which is closely related to the source of bubbles. The vortex structures in the OWB region are mainly induced by the air entrainment of the first impact and the successive splash-ups. When the falling jet moves forward and downward, the forward face of the wave is impacted, which induces the generation of the primary vortex structures. Splash-ups lead to the generation of secondary vortex structures. In addition, the air cavity is also wrapped by many vortex structures, which are discussed in more detail below.

Figure 18(a) presents a close sight of the vortex structures from the bottom view of the aerated cavity. Two mechanisms account for the vortex structures: one is the rotation of the air cavity, and another is the topological deformation of the interface. A significant pattern seen in region A is coherent structures that are regularly distributed and spaced along the air cavity. These strong organized structures are observed to coil and be parallel while they are wrapped around the air cavity. The rotating motion of the surrounding water is responsible for the generation of a sequence of large-scale coherent structures. The vortex structures are chaotic in the highly aerated region B, in which the air is dragged beneath free surface when vortices interact with the free surface in the wake region, producing strong turbulence with large numbers of bubbles. The spiraling flow is visualized by depicting the streamlines wrapped around the air cavity, as shown in Fig. 18(b). The arrows on the streamlines indicate the flow direction. The results suggest that the air cavity rolls from the outside to the inside, evolving along the cavity center axis, which is consistent with Fig. 4(b). In terms of the air entrainment process, the vortices induced by the air cavity deform the interface and result in the air entrainment. Meanwhile, at the rear of the cavity, the instability of the cavity interface promotes the generation of large-scale vortex structures.

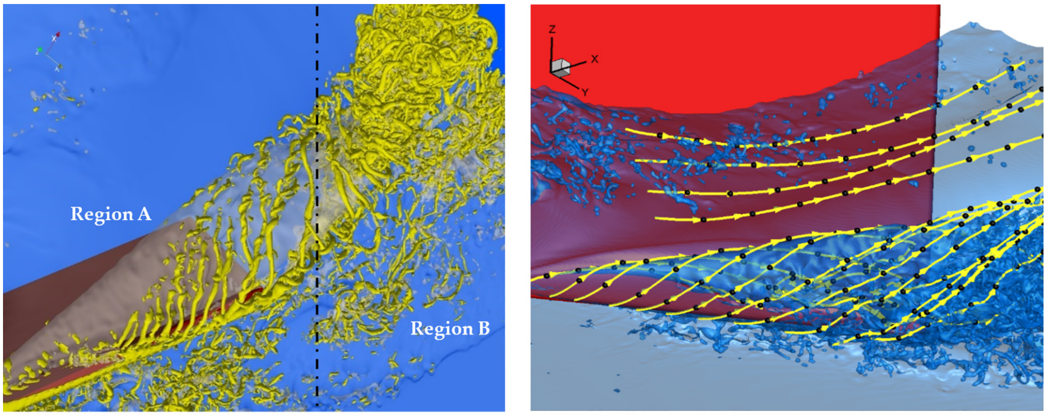

(a) (b)

FIG. 18. (a) Pictures showing the vortex structures wrapped around the air cavity (Region A) and in the wake (Region B) from the bottom view. (b) Streamlines spiraling around the aerated cavity, the arrows on the streamlines indicating the rotation direction of the air cavity. See Supplemental Material [60] for the whole flow process of streamlines.

IV. CONCLUSIONS

This paper focuses on the formation and development of the aerated cavity generated by a rectangular plate. A self-developed two-phase flow solver [4,5,49,57] is employed for the high-fidelity simulation, in which the fine flow structures associated with the physical process are resolved. The main geometrical characteristics of the air cavity with a series of yaw angles are summarized. With the bubble-droplet detection method [4], the overall distribution of the various sized bubbles generated by the breakups of air cavity is presented. With the use of state-of-the-art numerical techniques, the present numerical simulations improve our understanding for the air cavity induced by surface-piercing structures, which can be summarized as follows:

(1) For all cases, the air cavity is entrapped with stabilized rotational motion along the leading edge of the plate at yaw angles $\alpha_E \geqslant 35^\circ$. Reverse flow is observed in the depressed region owing to the blocking effect of the plate, which triggers two continuous opposite flows and produces vortices. Vortices with low strength are not enough to induce a stabilized and continuous air cavity. Rotating structures are thus clearly observed when the vortices are enough to overcome the gravity and surface tension of the interface. However, vortices that are too strong will steepen the wave plunger and force the air cavity to become more elliptical, resulting in a reduction of the air volume. The case $\alpha_E = 40^\circ$ shows the largest volume with moderate vortices. Meanwhile, a strong turbulence region is mainly related to the formation and breakup of the air cavity.

(2) Characteristic features of the air cavity under large yaw angles ($\alpha_E \geqslant 35^\circ$) depend strongly on the yaw angle. The length of the air cavity declines with the increase of the yaw angle. The cross-section of the air cavity has a larger penetration depth and a more elliptical shape as the yaw angle increases. For $\alpha_E \geqslant 40^\circ$, the volume of the entrapped air cavity decreases, owing to the shorter length and more elliptical profile as the yaw angle increases.

(3) The large-scale air cavity and the associated bubbles generated by it contribute much more air entrainment in the wake than that of the bow wave breaking. Meanwhile, from the contours of bubble size distribution $N(r,t)$, we find that the size of most of the bubbles in the wake is mainly concentrated in the range of 3–6 mm. The size distribution is not sensitive to the yaw angle, and the total count is dominated by small bubbles <4 mm, occupying 60% of the total number of bubbles at the stable stage for each case. The breakup of the air cavity and the interaction between the

entrapped bubbles in the later stage control the production of relatively small bubbles ($r < 4$ mm) and the resulting size distribution.

(4) Strong organized structures wrapped around the air cavity and many vortex structures in the wake are observed, which are closely related to the air entrainment. Two main reasons account for the generation of vortex structures: one is the rotation of the air cavity, and another is strong turbulence resulting from the topological deformation of the interface in the highly aerated wake region. The instability of the cavity promotes the generation of large-scale vortex structures.

ACKNOWLEDGMENT

This work is supported by the National Natural Science Foundation of China (Grants No. 51979160 and No. U2067220) and Top Young Talents of Ten Thousand Talents Plan, to which the authors are most grateful.

---

[1] F. Stern, Effects of waves on the boundary layer of a surface-piercing body, J. Ship Res. **30**, 256 (1986).

[2] F. Stern, J. E. Choi, and W. Hwang, Effects of waves on the wake of a surface-piercing flat plate: Experiment and theory, J. Ship Res. **37**, 102 (1993).

[3] E. M. Pogozelski, J. Katz, and T. T. Huang, The flow structure around a surface piercing strut, Phys. Fluids **9**, 1387 (1997).

[4] Y. D. Hu, C. Liu, C. H. Hu, and D. Wan, Numerical investigation of flow structure and air entrainment of breaking bow wave generated by a rectangular plate, Phys. Fluids **33**, 122113 (2021).

[5] Z. Li, C. Liu, D. C. Wan, and C. Hu, High-fidelity simulation of a hydraulic jump around a surface-piercing hydrofoil, Phys. Fluids **33**, 123304 (2021).

[6] W. Y. Chang, G. Constantinescu, and W. F. Tsai, Effect of array submergence on flow and coherent structures through and around a circular array of rigid vertical cylinders, Phys. Fluids **32**, 035110 (2020).

[7] T. A. Waniewski, C. E. Brennen, and F. Raichlen, Measurements of air entrainment by bow waves, J. Fluid Eng. **123**, 57 (2001).

[8] T. A. Waniewski, C. E. Brennen, and F. Raichlen, Bow wave dynamics, J. Ship Res. **46**, 1 (2002).

[9] Z. Y. Wang, J. M. Yang, and F. Stern, Numerical simulations of wave breakings around a wedge-shaped bow, in *Proceedings of 28th Symposium on Naval Hydrodynamics, Pasadena, California, USA* (NAP, Washington, DC, 2010).

[10] Z. Y. Wang, J. Suh, J. M. Yang, and F. Stern, Sharp interface LES of breaking waves by an interface piercing body in orthogonal curvilinear coordinates, in *Proceedings of 50th AIAA Aerospace Sciences Meeting including the New Horizons Forum and Aerospace Exposition, Nashville, Tennessee, USA* (AIAA, Reston, VA, 2012).

[11] K. Hendrickson and D. K.-P. Yue, Structures and mechanisms of air-entraining quasi-steady breaking ship waves, J. Ship Res. **63**, 69 (2019).

[12] K. Hendrickson, G. D. Weymouth, X. Yu, and D. K.-P. Yue, Wake behind a three-dimensional dry transom stern. Part 1. Flow structure and large-scale air entrainment, J. Fluid Mech. **875**, 854 (2019).

[13] K. Hendrickson and D. K.-P. Yue, Wake behind a three-dimensional dry transom stern. Part 2. Analysis and modelling of incompressible highly variable density turbulence, J. Fluid Mech. **875**, 884 (2019).

[14] R. Gomez-Ledesma, K. T. Kiger, and J. H. Duncan, The impact of a translating plunging jet on a pool of the same liquid, J. Fluid Mech. **680**, 5 (2011).

[15] C. Clanet, Plunging cavities, J. Fluid Mech. **680**, 1 (2011).

[16] Z. Y. Wang, J. M. Yang, and F. Stern, High-fidelity simulations of bubble, droplet and spray formation in breaking waves, J. Fluid Mech. **792**, 307 (2016).

[17] W. Mostert, S. Popinet, and L. Deike, High-resolution direct simulation of deep water breaking waves: Transition to turbulence, bubbles and droplet production, J. Fluid. Mech. **942**, A27 (2021).

[18] Q. Gao, G. B. Deane, and L. Shen, Bubble production by air filament and cavity breakup in plunging breaking wave crests, J. Fluid Mech. **929**, A44 (2021).

[19] L. Deike, W. K. Melville, and S. Popinet, Air entrainment and bubble statistics in breaking waves, J. Fluid Mech. **801**, 91 (2016).
[20] C. D. Ohl, H. N. Oguz, and A. Prosperetti, Mechanism of air entrainment by a disturbed liquid jet, Phys. Fluids **12**, 1710 (2000).
[21] S. H. Hassan, T. Guo, and P. P. Vlachos, Flow field evolution and entrainment in a free surface plunging jet, Phys. Rev. Fluids **4**, 104603 (2019).
[22] L. Deike, L. Lenain, and W. K. Melville, Air entrainment by breaking waves, Geophys. Res. Lett. **44**, 3779 (2017).
[23] K. T. Kiger and J. H. Duncan, Air-entrainment mechanisms in plunging jets and breaking waves, Annu. Rev. Fluid Mech. **44**, 563 (2012).
[24] P. Karnakov, S. Litvinov, J. M. Favre, and P. Koumoutsakos, Breaking waves: To foam or not to foam? Phys. Rev. Fluids **5**, 110503 (2020).
[25] C. Garrett, M. Li, and D. Farmer, The connection between bubble size spectra and energy dissipation rates in the upper ocean, J. Phys. Oceanogr. **30**, 2163 (2000).
[26] G. B. Deane and M. D. Stokes, Air entrainment processes and bubble size distributions in the surf zone, J. Phys. Oceanogr. **29**, 1393 (1999).
[27] G. B. Deane and M. D. Stokes, Scale dependence of bubble creation mechanisms in breaking waves, Nature (London) **418**, 839 (2002).
[28] W. Chan, S. Mirjalili, S. S. Jain, J. Urzay, A. Mani, and P. Moin, Birth of microbubbles in turbulent breaking waves, Phys. Rev. Fluids **4**, 100508 (2019).
[29] W. Chan, P. Johnson, and P. Moin, The turbulent bubble break-up cascade: Part 1. Theoretical developments, J. Fluid Mech. **912**, A42 (2021).
[30] W. Chan, P. Johnson, P. Moin, and J. Urzay, The turbulent bubble break-up cascade. Part 2. Numerical simulations of breaking waves, J. Fluid Mech. **912**, A43 (2021).
[31] P. Lubin and S. Glockner, Numerical simulations of three-dimensional plunging breaking waves: Generation and evolution of aerated vortex filaments, J. Fluid Mech. **767**, 364 (2015).
[32] Y. Watanabe, H. Saeki, and R. J. Hosking, Three-dimensional vortex structures under breaking waves, J. Fluid Mech. **545**, 291 (2005).
[33] D. Lakehal and P. Liovic, Turbulence structure and interaction with steep breaking waves, J. Fluid Mech. **674**, 522 (2011).
[34] S. Y. Yu, D. K.-P. Yue, L. Wang, and X. Yu, Direct numerical simulations of air entrainment induced by vortex structures, in *Proceedings of 28th International Ocean and Polar Engineering Conference, Sapporo, Japan* (ISOPE, Cupertino, California, 2018).
[35] F. Noblesse, D. Hendrix, L. Faul, and J. Slutsky, Simple analytical expressions for the height, location, and steepness of a ship bow wave, J. Ship Res. **50**, 360 (2006).
[36] F. Noblesse, G. Delhommeau, M. Guilbaud, D. Hendrix, and C. Yang, Simple analytical relations for ship bow waves, J. Fluid Mech. **600**, 105 (2008).
[37] G. Delhommeau, M. Guilbaud, L. David, C. Yang, and F. Noblesse, Boundary between unsteady and overturning ship bow wave regimes, J. Fluid Mech. **620**, 167 (2009).
[38] J. Smagorinsky, General circulation experiments with the primitive equations: I. The basic experiment, Mon. Weather Rev. **91**, 99 (1963).
[39] S. Vincent, J. Larocque, D. Lacanette, A. Toutant, P. Lubin, and P. Sagaut, Numerical simulation of phase separation and a priori two-phase LES filtering, Comput. Fluids **37**, 898 (2008).
[40] J. Larocque, S. Vincent, D. Lacanette, P. Lubin, and J.-P. Caltagirone, Parametric study of LES subgrid terms in a turbulent phase separation flow, Int. J. Multiphas. Flow **31**, 536 (2010).
[41] A. Toutant, M. Chandesris, D. Jamet, and O. Lebaigue, Jump conditions for filtered quantities at an under-resolved discontinuous interface. Part 1: Theoretical development, Int. J. Multiphas. Flow **35**, 1100 (2009).
[42] M. Saeedipour, S. Vincent, and S. Pirker, Jump conditions for filtered quantities at an under-resolved discontinuous interface. Part 1: Theoretical development, Int. J. Multiphas. Flow **112**, 286(2019).
[43] E. D. Christensen, Large eddy simulation of spilling and plunging breakers, Coast. Eng. **53**, 463 (2006).
[44] T. Cui, G. H. He, M. R. Jiang, W. Wang, L. Yuan, D. Han, A. Kamath, and H. Bihs, Large eddy simulation of focused breaking waves with different wave steepness, Ocean Model. **179**, 102122 (2022).

[45] F. Zhao, R. Wang, H. Zhu, H. Ping, Y. Bao, D. Zhou, Y. Cao, and H. Cui, Large-eddy simulations of flow past a circular cylinder near a free surface, Phys. Fluids **33**, 115108 (2021).
[46] B. Koo, Z. Y. Wang, J. M. Yang, and F. Stern, Impulsive plunging wave breaking downstream of a bump in a shallow water flume—Part II: Numerical simulations, J. Fluid. Struct. **32**, 121 (2012).
[47] A. J. Chorin, Numerical solution of the Navier-Stokes equations, Math. Comput. **22**, 745 (1968).
[48] M. Sussman and E. G. Puckett, A coupled level set and volume-of-fluid method for computing 3D and axisymmetric incompressible two-phase flows, J. Comput. Phys. **162**, 301 (2000).
[49] C. Liu, R. Q. Gao, and C. H. Hu, A consistent mass–momentum flux computation method for the simulation of plunging jet, Phys. Fluids **34**, 032114 (2022).
[50] Z. Li, C. Liu, R. Q. Gao, and C. Hu, A consistent mass-momentum advection method for the simulation of large-density-ratio two-phase flows, Int. J. Multiphas. Flow **156**, 104192 (2022).
[51] M. Sussman, K. M. Smith, M. Y. Hussaini, M. Ohta, and R. Zhi-Wei, A sharp interface method for incompressible two-phase flows, J. Comput. Phys. **221**, 469 (2007).
[52] C. Liu and C. H. Hu, A second order ghost fluid method for an interface problem of the Poisson equation, Comput. Phys. Commun. **22**, 965 (2017).
[53] C. Liu and C. H. Hu, An efficient immersed boundary treatment for complex moving object, J. Comput. Phys. **274**, 654 (2014).
[54] C. Liu and C. H. Hu, Block-based adaptive mesh refinement for fluid-structure interactions in incompressible flows, Comput. Phys. Commun. **232**, 104 (2018).
[55] C. Liu and C. H. Hu, Adaptive THINC-GFM for compressible multi-medium flows, J. Comput. Phys. **342**, 43 (2017).
[56] C. Liu and C. H. Hu, An adaptive multi-moment FVM approach for incompressible flows, J. Comput. Phys. **359**, 239 (2018).
[57] X. B. Yang, C. Liu, D. Wan, and C. H. Hu, Numerical study of the shock wave and pressure induced by single bubble collapse near planar solid wall, Phys. Fluids **33**, 073311 (2021).
[58] C.-W. Shu, High-order finite difference and finite volume WENO schemes and discontinuous Galerkin methods for CFD, Int. J. Comput. Fluid Dyn. **17**, 107 (2003).
[59] M. Mortazavi, G. V. Le, P. Moin, and A. Mani, Direct numerical simulation of a turbulent hydraulic jump: Turbulence statistics and air entrainment, J. Fluid Mech. **797**, 60 (2016).
[60] See Supplemental Material at http://link.aps.org/supplemental/10.1103/PhysRevFluids.8.044003 for a video, the detailed temporal and spatial evolution process of the aerated cavity, and the whole flow process of streamlines.
[61] G. Rojas and M. R. Loewen, Fiber-optic probe measurements of void fraction and bubble size distributions beneath breaking waves, Exp. Fluids **43**, 895 (2007).